Article:
Paspatis, A., Konstantopoulos, G. and Dedeoglu, S. (2021) Control design and small-signal stability analysis of inverter-based microgrids with inherent current limitation under extreme load conditions. Electric Power Systems Research, 193. 106929. ISSN: 0378-7796

https://doi.org/10.1016/j.epsr.2020.106929

Control Design and Small-Signal Stability Analysis of Inverter-Based Microgrids with Inherent Current Limitation under Extreme Load Conditions*

A.G. Paspatis[a], G.C. Konstantopoulos[a,b], S. Dedeoglu[a]

[a]*Dept. of Automatic Control and Systems Engineering, The University of Sheffield, Sheffield, S1 3JD, UK*
[b]*Dept. of Electrical and Computer Engineering, University of Patras, Rion, 26500, Greece*

Abstract

A novel droop controller that ensures a desired inverter current limitation and guarantees the stable operation of inverter-based microgrids under extreme load conditions, is proposed in this paper. Opposed to existing dq framework-based droop controllers that align the output voltage on d axis, here the inverter current is aligned on d axis in order to achieve two main goals: i) limitation of the RMS value of each inverter current during transients, without a need for saturation units that guarantee only steady-state limitation and require adaptation techniques for adjusting their limits and ii) a rigorous proof of closed-loop system stability for the entire microgrid. In particular, the proposed approach significantly simplifies the stability analysis of the microgrid, since it can be investigated through a Jacobian matrix of reduced size. Simulation results are given to highlight the superiority of the proposed controller when compared to a conventional droop controller under extreme load conditions, while experimental validation in a lab-scale microgrid is also provided.

Keywords: Nonlinear control systems, droop control, microgrid, small-signal stability analysis, current-limiting control, inverters

1. Introduction

The increasing penetration of distributed energy resources (DERs) in modern power systems has increased the interest in investigating the operation of microgrids in order to locally utilize the DER capabilities [1]. Since the majority of DERs use inverters for their integration to the power grid, the inverter-based microgrids concept has emerged, where crucial issues such as the proportional power sharing between DER units, the voltage and frequency regulation and the converter protection are required to be addressed through the control design [2, 3].

Among other control schemes, droop control can guarantee regulation of the load voltage and frequency close to their nominal values, without requiring any communication units, while proportional power sharing is also preserved when the inverters have the same per unit output impedance [3, 4, 5]. Hence, droop control has been the most widely used technique in inverter-based microgrids. Different droop controllers have been proposed in the literature in order to improve the system performance and stability [4, 6]. In most of the cases, the $Q-V$ and $P-f$ droop relations are considered, as they are defined by CERTS [7, 8], to mimic the operation of synchronous generators [9]. However, different droop relations are required when the output impedance is not inductive, while, recently, universal droop schemes have been proposed to handle different types of output impedance [4, 10].

Apart from the voltage and frequency regulation, closed-loop stability of inverter-based microgrids is of great importance as well. Analytical stability conditions have been presented in [11, 12], however several assumptions have been taken into consideration such as small or zero power angles, lossless lines or a time-scale separation between the inverters and the lines. Thus, to investigate stability around an equilibrium point, a root-locus analysis of the linearized system (small-signal model) is usually performed [3, 4, 13, 14].

The majority of works that deal with droop control and closed-loop system stability of inverter-based microgrids, examine the operation under normal load conditions. However, overload or faulty conditions occur very often and should be considered in power system studies [15, 16]. In the same context, due to the strict technical limitation in the maximum current of each inverter, current-limiting techniques should be embedded through the control design of every inverter-interfaced DER [17, 18, 19, 20]. In conventional cascaded control schemes, the current limitation is accomplished through saturation units in the inner control loops, which may suffer from integrator wind-up and eventually lead to instability [21], while adaptive saturation is required to allow maximum power

*This work is supported by EPSRC under Grants No EP/S001107/1 and EP/S031863/1.

Email addresses: apaspatis1@sheffield.ac.uk (A.G. Paspatis), g.konstantopoulos@sheffield.ac.uk (G.C. Konstantopoulos), sdedeoglu1@sheffield.ac.uk (S. Dedeoglu)

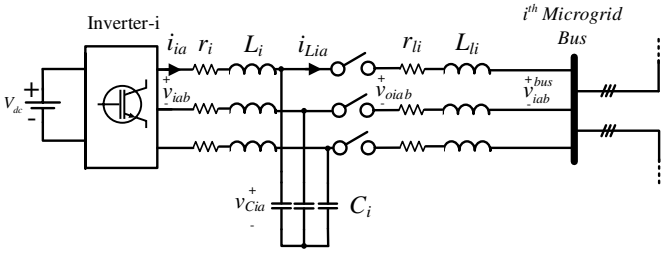

Figure 1: Inverter connected to a generic microgrid

utilization during faults [22, 23]. Another approach considers switching to a different current-limiting controller during faults. However, such an action can still suffer from integrator wind-up or force the controller to latch-up [21, 24, 25]. Moreover, these approaches guarantee a current limitation only at the steady-state. In order to overcome these undesirable phenomena, the virtual impedance or resistance concept offers a promising solution [21, 26]. To this end, a current-limiting droop control concept has been proposed in [25] for single-phase inverters, where no switching actions or saturated integrators are used to achieve the current limitation. However, this work considers the grid-connected operation of a single-phase inverter and the same control approach can not be directly applied to inverter-based microgrids.

In this paper, a new droop control approach that guarantees an inverter current limitation during transients and ensures stability for an entire inverter-based microgrid, is proposed. This is accomplished by aligning the inverter current on the d axis of the local (inverter) dq framework, in contrast to conventional droop control approaches that align the output voltage on the d axis [13]. It is analytically proven that the proposed control structure simplifies the Jacobian matrix, the eigenvalues of which should be computed in order to investigate the stability properties of an inverter-based microgrid. Hence, compared to conventional control techniques of droop-controlled inverters [22, 27], the novelties that the proposed controller brings include: 1) an inherent protection mechanism under extreme load conditions, which guarantees via the control design, a limited inverter current injection, even during transients, 2) limitation of the RMS value of the current below a desired value without requiring an adaptive limitation technique and 3) a Jacobian matrix of reduced size to study the stability properties of inverter-based microgrids that adopt the proposed control scheme. The superiority of the proposed controller is shown through comparative simulation results, while it is further validated through experimental results in a lab-scale microgrid.

2. Modeling and Motivation

2.1. Microgrid modeling

A generic inverter-dominated microgrid is considered in this paper, consisting of n three-phase inverters connected to the microgrid buses through an LC filter and an RL line, as depicted in Fig. 1. The power system components and variables are defined as follows: the inductance of the filter is denoted as L_i with its parasitic resistance being r_i, the filter capacitor is denoted as C_i, where i indicates the number of the inverter and the corresponding bus, with $i \in [1, \ldots, n]$. The line inductance and resistance are represented as L_{li} and r_{li}, respectively. The inverter voltage in the natural reference frame is defined as v_{iabc}, the inverter current is given as i_{iabc}, while the capacitor voltage, bus voltage and line current are represented as $v_{Ciabc}, v_{iabc}^{bus}$ and i_{Liabc}, respectively. Each inverter can measure its inverter current i_{iabc} and its point of common coupling (PCC) voltage v_{oiabc}. As it is clear from Fig. 1, when the inverter switches are open $v_{oiabc} = v_{iabc}^{bus}$, while when the switches close, $v_{oiabc} = v_{Ciabc}$. Following the synchronous reference frame theory [28], the dynamics of each inverter can be described in the synchronously rotating dq reference frame using θ_i as the angle of each inverter. Since in an inverter-based microgrid each individual inverter may have its own angle and hence, its own dq frame alignment, the local dq reference frame quantities (e.g. f_{dq}) of each DER with angular frequency ω_i, can be transformed into the global DQ reference frame quantities (e.g. f_{DQ}) with angular frequency ω_{com}, through the transformation

$$f_{DQ} = \begin{bmatrix} \cos\delta_i & -\sin\delta_i \\ \sin\delta_i & \cos\delta_i \end{bmatrix} f_{dq},$$

where δ_i is the rotational angle difference between the local reference frame of each DER and the global reference frame, given by

$$\dot{\delta}_i = \omega_i - \omega_{com}. \tag{1}$$

To facilitate the modeling, the angular frequency of one of the inverters can be selected as the global reference frame [13]. Following the above methodology, the considered microgrid can be modeled in the synchronous reference frame, where the dynamic equations for any of the n three-phase inverters of the microgrid are obtained as

$$L_i \frac{di_{id}}{dt} = v_{id} - v_{Cid} - r_i i_{id} + \omega_i L_i i_{iq} \tag{2}$$

$$L_i \frac{di_{iq}}{dt} = v_{iq} - v_{Ciq} - r_i i_{iq} - \omega_i L_i i_{id}, \tag{3}$$

where the inverter voltage components v_{id} and v_{iq} represent the control inputs. Note that the inverter real and reactive powers P_i and Q_i can be calculated from $P_i = 1.5\left(v_{Cid} i_{id} + v_{Ciq} i_{iq}\right)$ and $Q_i = 1.5\left(v_{Ciq} i_{id} - v_{Cid} i_{iq}\right)$. For the filter capacitors and each line that connects each PCC with the microgrid bus, the dynamics at the global reference frame rotating with ω_{com} [13, 29], take the form

$$C_i \frac{dv_{CiD}}{dt} = i_{iD} - i_{LiD} + \omega_{com} C_i v_{CiQ} \tag{4}$$

$$C_i \frac{dv_{CiQ}}{dt} = i_{iQ} - i_{LiQ} - \omega_{com} C_i v_{CiD} \tag{5}$$

$$L_{li} \frac{di_{LiD}}{dt} = v_{CiD} - v_{iD}^{bus} - r_{li} i_{LiD} + \omega_{com} L_{li} i_{LiQ} \tag{6}$$

$$L_{li} \frac{di_{LiQ}}{dt} = v_{CiQ} - v_{iQ}^{bus} - r_{li} i_{LiQ} - \omega_{com} L_{li} i_{LiD}. \tag{7}$$

2.2. Motivation

Droop control is widely used in inverter-based microgrids to enhance load voltage and frequency regulation and achieve proportional power sharing between DERs. However, the safe operation of microgrids under extreme load conditions should be also considered in the control design. In [25], a droop controller that offers an inherent current limitation for grid-connected inverter applications has been proposed. To accomplish this, the bounded integral controller (BIC) structure from [30] was employed to guarantee the boundedness of the control states. Nevertheless, there is a challenge in applying a rigorous current-limiting strategy in inverter-based microgrids, where the conventional approaches may lead to undesirable performance [24]. Furthermore, the microgrid stability analysis represents a far more challenging task than stability of inverters connected to a stiff grid and should be investigated [3, 28]. In the sequel of this paper, a novel current-limiting design of droop controllers will be proposed to facilitate the microgrid operation under extreme load conditions and ensure system stability.

3. The Proposed Controller: Control design and current-limiting property

3.1. Control Design

In order to accomplish the desired tasks highlighted in section 2.2, the proposed controller is suitably designed to align the inverter current on the d axis of each inverter local dq framework, to guarantee an inherent current limitation. To this end, the inverter voltage (which is the control input) consists of two parts: i) a voltage feed-forward term implemented in the abc reference frame and ii) a dynamic control part implemented in the dq reference frame. The proposed controller takes the form

$$v_{iabc} = v_{oiabc} + \overline{v}_{iabc}$$

where $\overline{v}_{iabc}$ is the dq to abc transformation of the reference voltages

$$\bar{v}_{id} = E_i - r_{vi} i_{id} - \omega_i L_i i_{iq} \tag{8}$$

$$\bar{v}_{iq} = -r_{vi} i_{iq} + \omega_i L_i i_{id}, \tag{9}$$

where E_i is a control state representing a virtual voltage, r_{vi} is a constant virtual resistance and $\omega_i L_i i_{iq}$ and $\omega_i L_i i_{id}$ are decoupling terms. The state E_i changes according to the nonlinear expressions

$$\dot{E}_i = c_i f_i(P_i, V_i) E_{qi}^2 \tag{10}$$

$$\dot{E_{qi}} = -\frac{c_i E_i E_{qi}}{E_{maxi}^2} f_i(P_i, V_i) - k_i \left(\frac{E_i^2}{E_{mi}^2} + E_{qi}^2 - 1 \right) E_{qi} \tag{11}$$

proposed in [30] while E_{qi} is an extra control state, c_i, k_i are positive constant gains and the control states initial conditions are defined as $E_{i0} = 0$, $E_{qi0} = 1$. The $P \sim V$, $Q \backsim -\omega$ droop expressions of the universal droop control scheme in [4] are considered here to provide robustness to different kinds of output impedance (i.e. resistive or capacitive). In the proposed controller, the function $f_i(P_i, V_i)$ inherits the real power droop control characteristics through the virtual voltage dynamics and takes the form

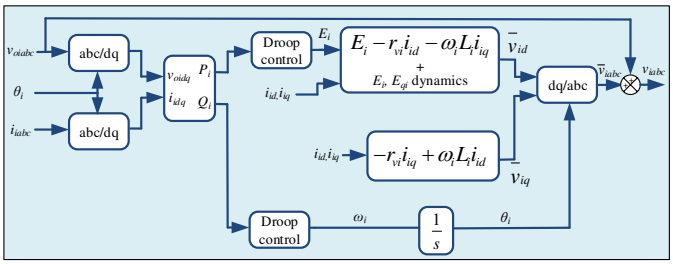

Figure 2: The proposed controller implementation

$$f_i(P_i, V_i) \quad = \quad E_{rms}^2 - V_i^2 - n_{pi} P_i. \tag{12}$$

The reactive power droop control is statically applied through the inverter local frequency ω_i with

$$\omega_i = \omega^* + m_{qi} Q_i, \tag{13}$$

while n_{pi}, m_{qi} represent the real power and reactive power droop coefficients, respectively, V_i is the RMS PCC voltage and E_{rms} is the nominal RMS load voltage. The proposed controller is depicted in Fig. 2. The BIC structure from [30] that was adopted for the controller dynamics (10)-(11), guarantees that the controller states E_i, E_{qi} will start and remain on the ellipse $W = \left\{ E_i, E_{qi} \in R : \frac{E_i^2}{E_{mi}^2} + E_{qi}^2 = 1 \right\}$, based on the given initial conditions. Thus it holds that $E_i \in [-E_{mi}, E_{mi}]$, with $E_{mi} > 0$ being the absolute maximum value of the control state, which is defined by the control operator and $E_{qi} \in [0, 1]$. For more details on the boundedness of the states E_i, E_{qi}, the reader is referred to [30]. This boundedness feature is essential for the desired inverter current-limiting property of any three-phase inverter connected to a microgrid, as it will be proven through the closed-loop system analysis in the sequel.

3.2. Current-limiting property

By applying the proposed controller (8)-(9) into the inverter current dynamics (2)-(3), and considering that the switches are closed, i.e. $v_{oiabc} = v_{Ciabc}$, the closed-loop system dynamics take the form

$$L_i \frac{di_{id}}{dt} \quad = \quad E_i - (r_{vi} + r_i)\, i_{id} \tag{14}$$

$$L_i \frac{di_{iq}}{dt} \quad = \quad -(r_{vi} + r_i)\, i_{iq}. \tag{15}$$

Note that at the steady state it holds $i_{ide} = \frac{E_i}{r_{vi} + r_i}$ and $i_{iqe} = 0$, while from (15), it is clear that if $i_{iq}(0) = 0$, then

$i_{iq}(t) = 0, \forall t \geq 0$. Now consider as Lyapunov function candidate the function

$$V = \frac{1}{2} L_i i_{id}^2 + \frac{1}{2} L_i i_{iq}^2.$$

Its time derivative takes the form

$$\dot{V} = \left(E_i i_{id} - (r_{vi} + r_i) i_{id}^2\right) - (r_{vi} + r_i) i_{iq}^2 \leq$$

$$[E_i \, 0] \begin{bmatrix} i_{id} \\ i_{iq} \end{bmatrix} - (r_{vi} + r_i) \left(i_{id}^2 + i_{iq}^2\right) \leq$$

$$- (r_{vi} + r_i) \left\| I_i \right\|_2^2 + \left\| \overline{E}_i \right\|_2 \left\| I_i \right\|_2,$$

where $I_i = [i_{id} \, i_{iq}]^T$ and $\overline{E}_i = [E_i \, 0]^T$. Furthermore taking into account the dq transformation where

$$\left\| I_i \right\|_2 = \sqrt{i_{id}^2 + i_{iq}^2} = \sqrt{2} I_{irms}$$

$$\left\| \overline{E}_i \right\|_2 = \sqrt{E_i^2} = |E_i|$$

and given that $|E_i| \leq E_{mi}$ from the BIC structure, as explained in the previous subsection, it follows that

$$\dot{V} \leq -2 (r_{vi} + r_i) I_{irms}^2 + \sqrt{2} E_{mi} I_{irms}$$

$$\dot{V} \leq -2 r_i I_{irms}^2, \forall I_{irms} \geq \frac{E_{mi}}{\sqrt{2} r_{vi}}.$$

Thus, according to the Theorem 4.18 in [31], there exists a $\mathcal{KL}$ function β so that for any initial condition $I_{irms}(0)$ there is a $T \geq 0$ such that

$$I_{irms}(t) \leq \beta \left(I_{irms}(0), t\right) \quad \forall 0 \leq t \leq T$$
$$I_{irms}(t) \leq \frac{E_{mi}}{\sqrt{2} r_{vi}} \qquad \forall t \geq T,$$

proving that the solution of the RMS inverter current is uniformly ultimately bounded. Note that if initially $I_{irms}(0) \leq \frac{E_{mi}}{\sqrt{2} r_{vi}}$, then $T = 0$, i.e. it holds true that

$$I_{irms}(t) \leq \frac{E_{mi}}{\sqrt{2} r_{vi}}, \forall t \geq 0. \tag{16}$$

By selecting the controller parameter $E_{mi} = \sqrt{2} I_{irms}^{max} r_{vi}$, (16) yields

$$I_{irms} \leq I_{irms}^{max}, \forall t \geq 0.$$

According to the ultimate boundedness analysis, the controller variable I_{irms}^{max} can be accordingly selected by the controller operator in order to ensure an inverter RMS current limitation at all times, even during transients. Moreover, since the ultimate bound I_{irms}^{max} is a constant and does not depend on the microgrid conditions, the maximum available power can be utilized under extreme load conditions, as required in the latest Grid Codes, without the need of online adaptation techniques.

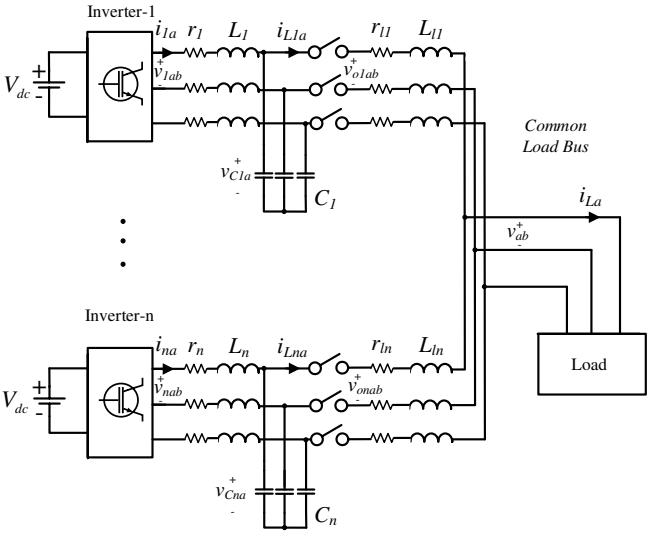

Figure 3: Microgrid under consideration for the small-signal stability analysis

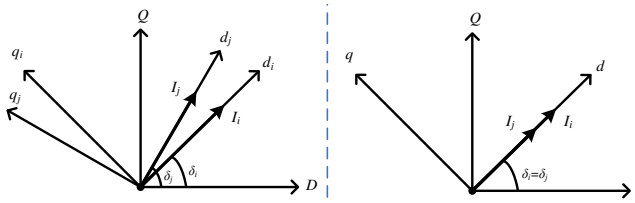

Figure 4: dq and DQ rotating frameworks under the proposed controller. Left: Angle transformation under generic topology. Right: Angle transformation in the case of a common load bus without lines

4. Small-signal stability analysis of common load bus inverter-based microgrid

4.1. The case without lines between the PCC and the load

Although, in the previous section, the desired RMS current limitation was proven for each inverter, the stability of the entire inverter-based microgrid is not yet guaranteed. This is a crucial problem due to the absence of a stiff grid to stabilize voltage and frequency [28]. For the stability analysis section, a common load bus microgrid will be considered, as depicted in Fig. 3. This microgrid configuration is commonly considered in power system stability studies [3, 19, 32], while as highlighted in [32], it represents a special case of a meshed microgrid. To investigate stability using the proposed a controller, a simple case will be initially considered where each inverter is directly connected to the load bus, i.e. without the lines shown in Fig. 3. This means that all inverters measure the same load voltage components in the global reference frame, i.e. by denoting any two inverters as i and j, it holds $v_{CiD} = v_{CjD} = v_D$ and $v_{CiQ} = v_{CjQ} = v_Q$. Taking into account the angle difference of each inverter from (1) and since it is proven in Section 3.2 that $i_{iq} = 0$, one can rewrite the power equations as $P_i = 1.5(v_D \cos\delta_i + v_Q \sin\delta_i) i_{id}$ and $Q_i = 1.5(v_Q \cos\delta_i - v_D \sin\delta_i) i_{id}$. Since the same RMS voltage is measured by every inverter, then accurate power

sharing will be achieved for both real and reactive power at the steady-state. Hence, it holds that $\frac{n_{pi}}{n_{pj}} = \frac{P_j}{P_i}$ and $\frac{m_{qi}}{m_{qj}} = \frac{Q_j}{Q_i}$, with $\frac{n_{pi}}{n_{pj}} = \frac{m_{qi}}{m_{qj}}$. Thus, at the steady-state

$$\begin{aligned} n_{pi} i_{id} \left(v_D \cos\delta_i + v_Q \sin\delta_i\right) &= n_{pj} i_{jd} \left(v_D \cos\delta_j + v_Q \sin\delta_j\right) \\ m_{qi} i_{id} \left(v_Q \cos\delta_i - v_D \sin\delta_i\right) &= m_{qj} i_{jd} \left(v_Q \cos\delta_j - v_D \sin\delta_j\right), \end{aligned}$$

which by dividing these two equations and after some manipulations results to $\left(v_D^2 + v_Q^2\right) \sin\left(\delta_j - \delta_i\right) = 0$. Under the common assumption that $\delta_i, \delta_j \in \left(-\frac{\pi}{2}, \frac{\pi}{2}\right)$ [11], it is concluded that $\delta_i = \delta_j$.

This proof shows that in the absence of lines between the PCC of each inverter and the common load bus, not only accurate power sharing is achieved without the need of hierarchical control structures but also, the rotational angle differences δ_i and δ_j are all the same and hence, by selecting the angular frequency of one inverter as the global reference frame, it holds $\delta_i = \delta_j = 0$ at the steady-state. This is also graphically explained in Fig. 4. However, since this represents only a special case, an analysis considering the entire microgrid with the lines, as depicted in Fig. 3, will be performed in the next subsection.

4.2. The case with resistive-inductive lines between the PCC and the load bus

The state vector of the closed-loop system, when lines are considered between the PCC of each inverter and the common load (where the angle difference δ_i can not be ignored), as shown in Fig. 3, becomes $x = [i_{1d} ... i_{nd}\, E_1 ... E_n\, v_{C1D} ... v_{CnD}\, v_{C1Q} ... v_{CnQ}\, i_{L1D} ... i_{LnD} i_{L1Q} ... i_{LnQ}\, \delta_2 ... \delta_n\, E_{q1} ... E_{qn}\, i_{1q} ... i_{nq}]^T$, where the load is modeled as constant impedance load (RL) with the load current denoted as i_{Labc}. Moreover, the angular frequency of the first inverter is selected as the frequency of the global reference frame, i.e. $\omega_1 = \omega_{com}$. Note that when considering a constant impedance load, as commonly done in power system studies [13], the load dynamics take the form

$$\begin{aligned} L\frac{di_{LD}}{dt} &= v_D - Ri_{LD} + \omega_{com} L i_{LQ} \\ L\frac{di_{LQ}}{dt} &= v_Q - Ri_{LQ} - \omega_{com} L i_{LD}. \end{aligned}$$

For the coupling terms in the system dynamics and the rotational angle dynamics, the angular frequency of the global reference frame is selected as the steady-state microgrid frequency to simplify the analysis, as in [13, 29]. Considering an equilibrium point x_e with $x_e = [i_{1de} ... i_{nde} E_{1e} .. .E_{ne} v_{C1De} ... v_{CnDe} v_{C1Qe} ... v_{CnQe} i_{L1De} ... i_{LnDe} i_{L1Qe} ... i_{LnQe}\, \delta_{2e} ... \delta_{ne}\, E_{q1e} ... E_{qne}\, i_{1qe} ... i_{nqe}]^T$, where $|E_{ie}| < E_{mi}$ and $E_{qie} \in (0, 1]$, the Jacobian matrix, which is obtained by linearizing the closed-loop system, takes the form

$$A = \begin{bmatrix} A_T & 0 & A_2 \\ A_1 & -diag\left\{2k_i E_{qie}^2\right\} & A_3 \\ 0 & 0 & -diag\left\{\frac{r_{vi}+r_i}{L_i}\right\} \end{bmatrix}. \quad (18)$$

Hence, according to the small-signal analysis, the closed-loop system will be stable if all the eigenvalues of the matrix A_T in (17) have negative real parts, where it holds $\kappa_i = \left(v_{CiDe} \cos\delta_{ie} + v_{CiQe} \sin\delta_{ie}\right)$, $\lambda_i = \left(\cos\delta_{ie} v_{CiDe} + \sin\delta_{ie} v_{CiQe}\right)$ and the submatrices of the matrix A_T are given in the Appendix.

Remark 1. It should be highlighted that the dynamics of the currents i_{iq} have been decoupled under the proposed control scheme, as it is clear from (18). Hence, the stability investigation can be performed through a new Jacobian matrix A_T which is reduced by n states compared to conventional SRF-based droop controllers. In the conventional approaches, the voltage v_{Ciq} is regulated to zero [13] and a different timescale for the inner current controller has to be assumed in order to achieve a similar simplification in the Jacobian matrix and decouple the voltage dynamics. Moreover, it is clear that this simplification is achieved irrespective to the microgrid topology, which only affects the matrix A_T, hence it holds for a generic meshed microgrid as well. Thus, with the proposed control scheme the Jacobian matrix, and concurrently the microgrid stability analysis, is significantly simplified, without considering any timescale separation assumption.

4.3. Identifying the equilibrium point and root-locus analysis

In order to perform a root-locus analysis, the steady-state equilibrium point of the entire microgrid needs to be identified. However, the analytic calculation of the equilibrium point is a daunting task when dealing with islanded microgrids [13, 33] and hence, many papers approximate the required equilibrium points through time-domain simulations [33, 34, 35]. Note that an exemplary microgrid with two inverters will be considered for simplicity but a similar methodology can be followed for any number of inverters, since the modeling in the previous subsections deals with the case of n inverters. Firstly, the first inverter's angular frequency is selected as the global reference frame. Then, only the values of I_{1rms} and ω_{com} are needed to be identified. Thus, keeping in mind that $\delta_1 = 0$, then $i_{1de} = i_{1De} = \sqrt{2} I_{1rms}$ and $i_{1qe} = i_{1Qe} = 0$. Now, the capacitor voltages of the first inverter can be calculated from the droop expressions at the steady-state as

$$\begin{aligned} v_{C1Qe} &= \frac{\omega_{com} - \omega^*}{1.5 m_{q1} i_{1De}} \\ v_{C1De} &= \sqrt{2.25 n_{p1}^2 i_{1De}^2 - v_{C1Qe}^2 + 2E_{rms}^2} - 1.5 n_{p1} i_{1De} \end{aligned}$$

and the line currents of the first inverter can be obtained from the steady-state equation of the capacitor dynamics

$$\begin{aligned} i_{LiDe} &= i_{iDe} + \omega_{com} C_i v_{CiQe} \quad (19) \\ i_{LiQe} &= i_{iQe} - \omega_{com} C_i v_{CiDe} \quad (20) \end{aligned}$$

for $i \in \{1, 2\}$. Following the analysis in [32], the admittance matrix for the setup under consideration in the DQ framework takes the form

$$\begin{bmatrix} i_{L1De} \\ i_{L1Qe} \\ i_{L2De} \\ i_{L2Qe} \end{bmatrix} = \begin{bmatrix} G_{11} & -B_{11} & G_{12} & -B_{12} \\ B_{11} & G_{11} & B_{12} & G_{12} \\ G_{12} & -B_{12} & G_{22} & -B_{22} \\ B_{12} & G_{12} & B_{22} & G_{22} \end{bmatrix} \begin{bmatrix} v_{C1De} \\ v_{C1Qe} \\ v_{C2De} \\ v_{C2Qe} \end{bmatrix}.$$

Through the admittance matrix, the values of v_{C2De}, v_{C2Qe} and i_{L2De}, i_{L2Qe} can be calculated, and at the same time using the steady-state capacitor equations (19)-(20) of the second inverter, the inverter currents in the global frame can be obtained as well. Finally, since it holds that $\delta_2 =$

$$A_T = \begin{bmatrix} -diag\left\{\frac{r_{vi}+r_i}{L_i}\right\} & diag\left\{\frac{1}{L_i}\right\} & 0_{n\times 2n} & 0_{n\times 2n} & 0_{n\times(n-1)} \\ -diag\left\{c_i n_{pi} E_{qie}^2 \frac{3}{2}\kappa_i\right\} & 0_{n\times n} & A_{T1} & 0_{n\times 2n} & A_{T2} \\ A_{T3} & 0_{2n\times n} & \begin{bmatrix} 0_{n\times n} & diag\{\omega_{com}\} \\ -diag\{\omega_{com}\} & 0_{n\times n} \end{bmatrix} & \begin{bmatrix} -diag\left\{\frac{1}{C_i}\right\} & 0_{n\times n} \\ 0_{n\times n} & -diag\left\{\frac{1}{C_i}\right\} \end{bmatrix} & A_{T4} \\ 0_{2n\times n} & 0_{2n\times n} & A_{T5} & A_{T6} & 0_{2n\times(n-1)} \\ A_{T7} & 0_{(n-1)\times n} & A_{T8} & 0_{(n-1)\times 2n} & -diag\{m_{qi}\frac{3}{2} i_{ide}\lambda_i\} \end{bmatrix} \quad (17)$$

$acos\left(i_{2D}/\sqrt{i_{2D}^2+i_{2Q}^2}\right)$, the inverter currents of the second inverter in their local frame can be found as well, while it holds that $E_{ie} = i_{ide}\,(r_{vi}+r_i)$ and $E_{qie}=\sqrt{1-(E_{ie}^2/E_{mi}^2)}$ from the BIC analysis. A specific equilibrium point for a constant RL load can now be finally obtained using the system parameters given in Table 1. The calculated equilibrium point is also given in Table 1.

In Fig. 5, the eigenvalues of the closed-loop system, for the considered equilibrium point, are depicted for controller gains $c_1 = c_2$ ranging from 0.02 to 1.2. It is shown that up to a value of $c_{critical} = 1.02$, all the eigenvalues have negative real parts and thus, the microgrid is stable around the considered equilibrium point using the proposed control approach. Hence, c_i can be selected according to the root-locus analysis to obtain the desired transient response and guarantee closed-loop system stability.

Even though the above stability analysis leads to a local stability result, as commonly achieved using small-signal modeling, it is underlined that the boundedness of the current of any inverter in the microgrid (proven in Section 3.2) is guaranteed for the original nonlinear model, in contrary to the majority of existing microgrid stability approaches which are restricted to local results only. Moreover, for the considered microgrid topology in Fig. 3, one can easily show for the original nonlinear system that due to the current boundedness, the rest of the system states (capacitor voltages, line currents and load currents) will remain bounded as well [25].

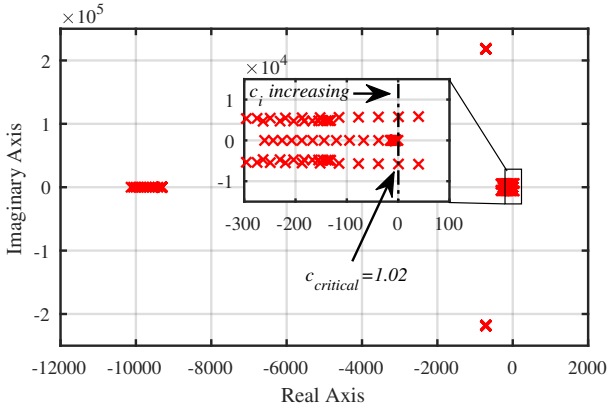

Figure 5: Closed-loop system eigenvalues for c_i ranging from 0.02 to 1.2

5. Comparison through Simulation Results

5.1. Selection of the benchmark controller

In order to validate the properties of the proposed controller, in this section, it will be compared with a conventional virtual resistance-based droop controller [3]. The widely used framework with inner voltage and current control loops will be considered for the conventional control scheme, with saturation units being applied to the reference inverter currents for current-limiting purposes, in a similar way as in [13, 21]. Finally, the selection of the droop coefficients is carried out according to the formulas in [13]. The control scheme discussed above is selected as the benchmark controller for the comparative simulations of the next subsection, and is depicted in Fig 6.

5.2. Simulation Results

To provide an insight into the performance of the proposed controller, compared to that of the benchmark controller, Matlab/Simulink simulation results are presented in this subsection. The exemplary case of two inverters that was used for the root-locus analysis is again considered, with Inverter #1 having twice the power rating of Inverter #2. The droop coefficients in the proposed controller can be selected as $n_{pi} = 0.19\frac{E_{rms}^2}{S_{maxi}}$ and $m_{qi} = 0.05\frac{\omega^*}{S_{maxi}}$, in order to allow a maximum of 10 % voltage deviation and 5 % frequency deviation. The power system and controller parameters are given in Table 1. For both control schemes the same scenario is examined: Initially both inverters do not feed the load since their switches are open. At 0.1 s, Inverter #1 is connected to the constant RL load which initially has the values of $R = 25\Omega$ and $L = 40$ mH, per phase. At 1.5 s, an extra load of $R = 25\,\Omega$ and $L = 40$ mH per phase is added in parallel to the initial one. At 3 s, Inverter #2 is connected and the two inverters share the common load. Finally, at 5 s, a three-phase short circuit is applied at the load bus, which is self-cleared after 150 ms.

Comparing the response of the two control schemes, depicted in Fig. 7, one can see that the singe inverter operation is similar for both schemes. However, at the time when Inverter #2 connects to the microgrid, the transient is much smoother using the proposed controller while using the benchmark controller, the Inverter #2 current rises close to its limit. The small difference in the power values comes from the fact that the benchmark controller powers are measured using the line current. When the three-phase short circuit is applied, using the benchmark

Table 1: Power system parameters, controller parameters and considered equilibrium point for root-locus analysis and comparative simulation results

Parameters	Values	Parameters	Values
Power system parameters			
L_1, L_2	2.2 mH	r_1, r_2	0.5 Ω
L_{l1}	0.028 mH	L_{l2}	0.014 mH
C_1, C_2	1 μF	r_{l1}, r_{l2}	0.04 Ω,0.02 Ω
R	12.5 Ω	L	20 mH
E_{rms}	220 V	ω^*	2π50 rad/s
I_{1rms}^{max}	20 A	I_{2rms}^{max}	10 A
S_{max1}	13.2 KVA	S_{max2}	6.6 KVA
Proposed controller parameters			
c_1, c_2	0.9	r_{v1}, r_{v2}	20 Ω
n_{p1}, n_{p2}	0.69, 1.39	m_{q1}, m_{q2}	0.0012, 0.0024
Benchmark controller parameters			
$k_{pi}, k_{ii}, k_{pv}, k_{iv}$	4, 200, 0.3, 12	r_{v1}, r_{v2}	0.7 Ω, 1.4 Ω
n_{p1}, n_{p2}	0.0047, 0.0094	m_{q1}, m_{q2}	0.0012, 0.0024
Considered equilibrium point			
v_{C1De}, v_{C1Qe}	266.52 V,134.08 V	v_{C2De}, v_{C2Qe}	266.11 V,133.99 V
i_{1de}, i_{2de}	13.97 A,7.18 A	i_{1qe}, i_{2qe}	0 A,0 A
i_{L1De}, i_{L1Qe}	14.01 A,−0.08 A	i_{L2De}, i_{L2Qe}	7.22 A,0.01 A
ω_{com}	317.50 rad/s	δ_{2e}	0.76 ^{o}

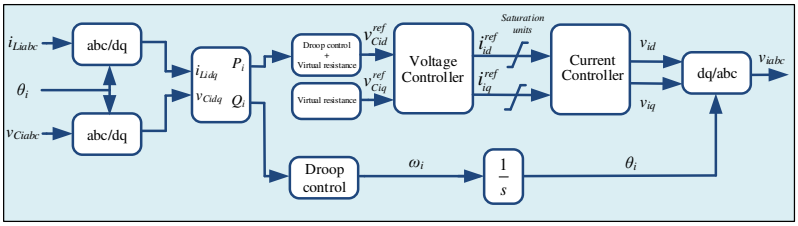

Figure 6: The benchmark controller implementation

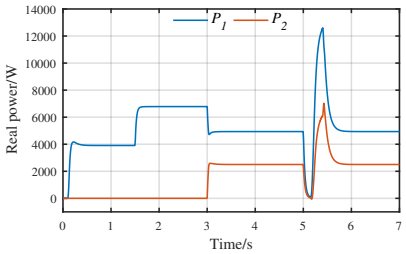

(a) Real power: Benchmark controller

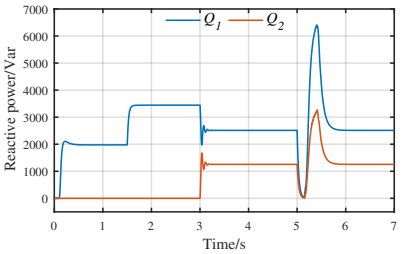

(b) Reactive power: Benchmark controller

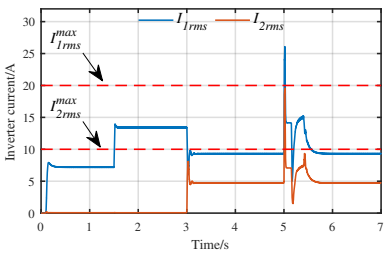

(c) Inverter currents: Benchmark controller

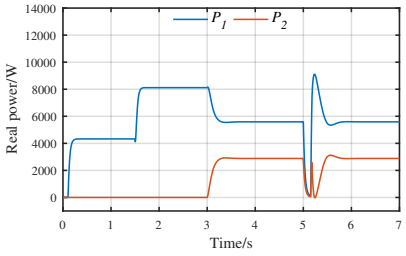

(d) Real power: Proposed controller

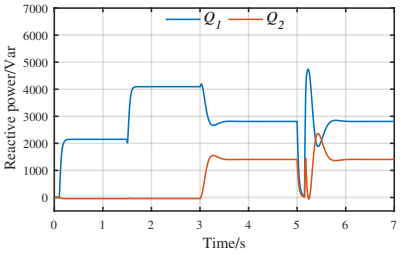

(e) Reactive power: Proposed controller

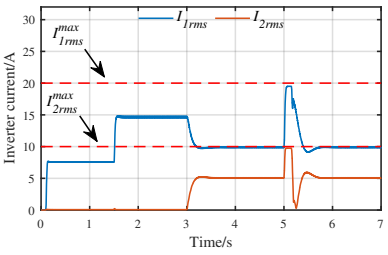

(f) Inverter currents: Proposed controller

Figure 7: Comparative simulation results

Table 2: System parameters for experimental results

Parameters	Values	Parameters	Values
L_1	3.5 mH	L_2	5.7 mH
L_{l1}	4.4 mH	L_{l2}	1 mH
r_1	0.4 Ω	r_2	0.8 Ω
r_{l1}	0.9 Ω	r_{l2}	0.4 Ω
C_1, C_2	1 μF	c_1, c_2	0.6
E_{rms}	90 V	ω^*	2π50 rad/s
I_{1rms}^{max}	2 A	I_{2rms}^{max}	1 A
k_1,k_2	1000	r_{v1}, r_{v2}	50 Ω, 10 Ω

controller, the inverter currents violate their limits during the transient and reach high values, even if their reference values are saturated. Moreover, during the steady-state, the maximum allowed current is not injected since in this certain example, i_{iq} takes very small values. For this issue to be solved, an adaptive saturation technique would be required which, however, further complicates the control implementation. On the other hand, using the proposed controller, both RMS inverter currents are driven to their maximum values without violating this threshold value, even during the transient. Even if both control schemes maintain a stable operation, the presented simulation results verify the superiority of the proposed controller in terms of its current-limiting capability and the maximum power utilization under faults.

6. Experimental Validation

A 90 V, 50 Hz prototype lab-scale microgrid was built in order to experimentally verify the proposed controller. The microgrid consists of two three-phase inverters with ratings of 540 VA for the first inverter (Inverter #1) and 270 VA for the second inverter (Inverter #2). The controllers were digitally implemented through a Texas Instruments (TI) F28M379D control card for Inverter #1 and a dSpace 1104 control card for Inverter #2, with 15 kHz sampling frequency. Both inverters were connected to a three-phase resistive load (R) through an LC filter and a inductive-resistive line, as shown in Fig. 3, while the system and controller parameters are given in Table 2.

Firstly, Inverter #1 is connected to the load, which is initially $R = 100\,\Omega$. As it can bee seen in Fig. 8, Inverter #1 regulates its output real power to feed the load, while regulating the voltage close to its nominal value E_{rms}. I_{1rms} is also depicted in the same figure. At 44 s, Inverter #2 is switched on and at 46 s, it starts its synchronization process by feed-forwarding the PCC voltage. The synchronization process can be clearly depicted in Fig. 9, where at 62 ms, the voltage read at the PCC is feed-forwarded at the inverter capacitors to allow a seamless connection. When the synchronization has been completed, at 49 s in Fig. 8, Inverter #2 is smoothly connected to the microgrid. In Fig. 10 the load voltage under the parallel operation of the two inverters is shown. Since the rating of Inverter #1

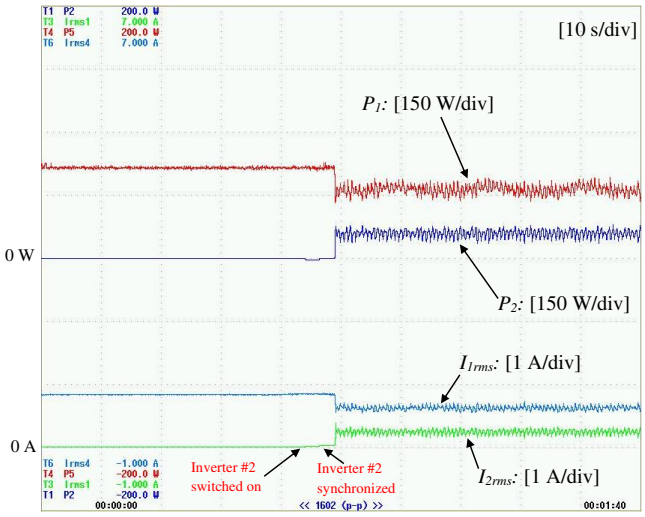

Figure 8: Initial operation of Inverter #1 and connection of Inverter #2

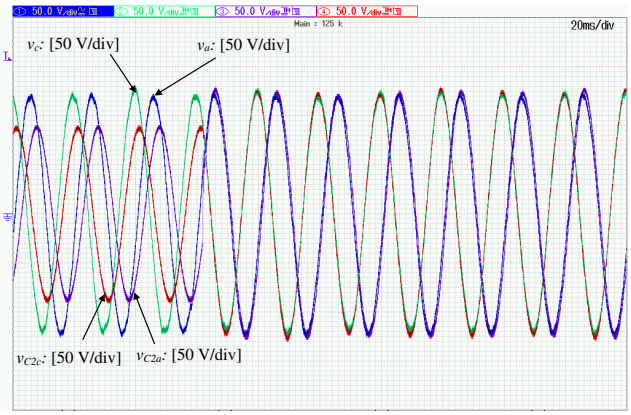

Figure 9: Synchronization process of Inverter #2

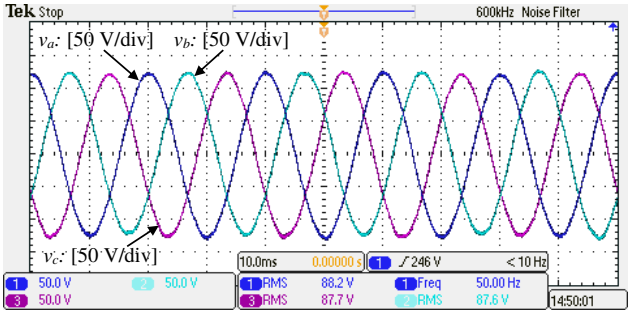

Figure 10: Load voltage under parallel operation of inverters

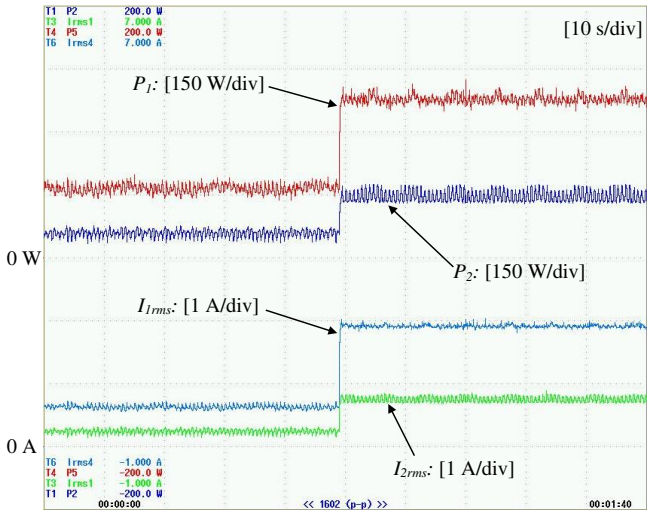

Figure 11: Load change and current-limiting property

is twice the rating of Inverter #2, a 2 : 1 power sharing is desired through the droop control. As it is illustrated in Fig. 8, the real powers and RMS currents of the two inverters are very close to the desired 2 : 1 sharing, where the small inaccuracies are expected due to the different line impedance ("line impedance effect"). Note that since the capacitors of the LC filter have small capacitance and the load is purely resistive, the reactive powers of both inverters are very close to 0 Var and thus, they are not presented here. Nevertheless, the effectiveness of the proposed controller under reactive power demand has been highlighted in the simulation results of Section 5.2.

To verify the inherent current-limiting property (that was analytically proven in Subsection 3.2), in Fig. 11, a load change from $R = 100\,\Omega$ to $R = 25\,\Omega$ is performed at 49 s, which represents an extreme loading demand condition. Following to the load change, I_{1rms} and I_{2rms} go very fast close to their maximum values (2 A and 1 A, respectively) without violating their limit at any time, even during the transient. Since the current provision is not enough to regulate the load voltage inside the selected 10% droop percentage, the load voltage drops to 70 V. The transient of the load voltage at the time that the load changes can be seen in Fig. 12, while i_{La} is also shown in the same figure. Note that the load current never exceeds the sum of the maximum RMS values of the two inverter currents, i.e. 3 A, even during the transient. This clearly demonstrates the current-limiting capability of the proposed controller for each inverter in the AC microgrid.

7. Conclusions

A new droop controller for inverter-based microgrids is proposed in this paper to inherently guarantee RMS inverter current limitation and microgrid stability. The proposed control scheme aligns the inverter current on the d axis of the local dq frame in order to rigorously prove

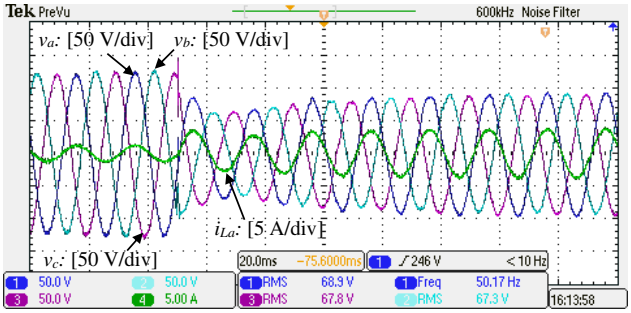

Figure 12: Load voltage and current transient during load change

the desired current limitation during transients and the stability of an entire microgrid. In particular, it is shown that through the proposed controller, the microgrid stability properties can be investigated through a Jacobian matrix of reduced size. The proposed control approach is compared to a conventional droop control scheme under extreme load conditions through simulation results, while its effectiveness is also verified experimentally in a prototype microgrid.

Future research will focus on the integration of secondary control schemes into the proposed controller and the development of tools for investigating global asymptotic stability of inverter-based microgrids.

Appendix

$$A_{T1} = \begin{bmatrix} c_1 E_{q1e}^2 \beta_1 & \cdots & 0 & -c_1 E_{q1e}^2 \gamma_1 & \cdots & 0 \\ \vdots & \ddots & \vdots & \vdots & \ddots & \vdots \\ 0 & \cdots & c_n E_{qne}^2 \beta_n & 0 & \cdots & -c_n E_{qne}^2 \gamma_n \end{bmatrix},$$

$$\beta_i = \left(-\tfrac{3}{2} n_{pi} i_{ide} \cos\delta_{ie} - v_{CiDe}\right),\ \gamma_i = \left(\tfrac{3}{2} n_{pi} i_{ide} \sin\delta_{ie} + v_{CiQe}\right).$$

$$A_{T2} = \begin{bmatrix} 0 & \cdots & 0 \\ c_2 n_{p2} E_{q2e}^2 \tfrac{3}{2} i_{2de} \eta_2 & \cdots & 0 \\ \vdots & \ddots & \vdots \\ 0 & \cdots & c_n n_{pn} E_{qne}^2 \tfrac{3}{2} i_{nde} \eta_n \end{bmatrix},$$

$$\eta_i = \left(-\cos\delta_{ie} v_{CiQe} + \sin\delta_{ie} v_{CiDe}\right).$$

$$A_{T3} = \begin{bmatrix} \frac{\cos\delta_{1e}}{C_1} & \cdots & 0 \\ \vdots & \ddots & \vdots \\ 0 & \cdots & \frac{\cos\delta_{ne}}{C_n} \\ \frac{\sin\delta_{1e}}{C_1} & \cdots & 0 \\ \vdots & \ddots & \vdots \\ 0 & \cdots & \frac{\sin\delta_{ne}}{C_n} \end{bmatrix}, A_{T4} = \begin{bmatrix} 0 & \cdots & 0 \\ -\frac{\sin\delta_{2e} i_{2de}}{C_2} & \cdots & 0 \\ \vdots & \ddots & \vdots \\ 0 & \cdots & -\frac{\sin\delta_{ne} i_{nde}}{C_n} \\ 0 & \cdots & 0 \\ \frac{\cos\delta_{2e} i_{2de}}{C_2} & \cdots & 0 \\ \vdots & \ddots & \vdots \\ 0 & \cdots & \frac{\cos\delta_{ne} i_{nde}}{C_n} \end{bmatrix}.$$

$$A_{T5} = \begin{bmatrix} \varrho_1 & \xi_{12} & \cdots & \xi_{1n} & 0 & 0 & \cdots & 0 \\ \xi_{21} & \varrho_2 & \cdots & \xi_{2n} & 0 & 0 & \cdots & 0 \\ \vdots & \vdots & \ddots & \vdots & \vdots & \vdots & \ddots & \vdots \\ \xi_{n1} & \xi_{n2} & \cdots & \varrho_n & 0 & 0 & \cdots & 0 \\ 0 & 0 & \cdots & 0 & \varrho_1 & \xi_{12} & \cdots & \xi_{1n} \\ 0 & 0 & \cdots & 0 & \xi_{21} & \varrho_2 & \cdots & \xi_{2n} \\ \vdots & \vdots & \ddots & \vdots & \vdots & \vdots & \ddots & \vdots \\ 0 & 0 & \cdots & 0 & \xi_{n1} & \xi_{n2} & \cdots & \varrho_n \end{bmatrix},$$

$\varrho_i = L_{li}^{-1} - \frac{L_{li}^{-2}}{L_{sum}^{-1}}$, $\xi_{ij} = -\frac{L_{li}^{-1} L_{lj}^{-1}}{L_{sum}^{-1}}$, $L_{sum}^{-1} = L^{-1} + \sum_{i=1}^{n} L_{li}^{-1}$.

$$A_{T6} = \begin{bmatrix} \varphi_1 & \psi_{12} & \cdots & \psi_{1n} & \omega_{com} & 0 & \cdots & 0 \\ \psi_{21} & \varphi_2 & \cdots & \psi_{2n} & 0 & \omega_{com} & \cdots & 0 \\ \vdots & \vdots & \ddots & \vdots & \vdots & \vdots & \ddots & \vdots \\ \psi_{n1} & \psi_{n2} & \cdots & \varphi_n & 0 & 0 & \cdots & \omega_{com} \\ -\omega_{com} & 0 & \cdots & 0 & \varphi_1 & \psi_{12} & \cdots & \psi_{1n} \\ 0 & -\omega_{com} & \cdots & 0 & \psi_{21} & \varphi_2 & \cdots & \psi_{2n} \\ \vdots & \vdots & \ddots & \vdots & \vdots & \vdots & \ddots & \vdots \\ 0 & 0 & \cdots & -\omega_{com} & \psi_{n1} & \psi_{n2} & \cdots & \varphi_n \end{bmatrix},$$

$\varphi_i = -L_{li}^{-1} \frac{L^{-1} R - L_{li}^{-1} r_{li}}{L_{sum}^{-1}} - L_{li}^{-1} r_{li}$, $\psi_{ij} = -L_{li}^{-1} \frac{R L^{-1} - L_{lj}^{-1} r_{lj}}{L_{sum}^{-1}}$.

$$A_{T7} = \begin{bmatrix} 0 & -m_{q2}\frac{3}{2}\eta_2 & \cdots & 0 \\ \vdots & \vdots & \ddots & \vdots \\ 0 & 0 & \cdots & -m_{qn}\frac{3}{2}\eta_n \end{bmatrix}.$$

$$A_{T8} = \begin{bmatrix} 0 & -\frac{3}{2}\zeta_2 & \cdots & 0 & 0 & \frac{3}{2}\sigma_2 & \cdots & 0 \\ \vdots & \vdots & \ddots & \vdots & \vdots & \vdots & \ddots & \vdots \\ 0 & 0 & \cdots & -\frac{3}{2}\zeta_n & 0 & 0 & \cdots & \frac{3}{2}\sigma_n \end{bmatrix},$$

$\zeta_i = m_{qi} i_{ide} \sin\delta_{ie}$, $\sigma_i = m_{qi} i_{ide} \cos\delta_{ie}$.

References

[1] T. Green, M. Prodanovic, Control of inverter-based micro-grids, Electric Power Systems Research 77 (9) (2007) 1204 – 1213, distributed Generation. doi:https://doi.org/10.1016/j.epsr.2006.08.017.

[2] Y. Xue, J. M. Guerrero, Smart inverters for utility and industry applications, in: Proceedings of PCIM Europe 2015; International Exhibition and Conference for Power Electronics, Intelligent Motion, Renewable Energy and Energy Management, 2015, pp. 1–8.

[3] J. M. Guerrero, J. Matas, L. G. de Vicuna, M. Castilla, J. Miret, Decentralized control for parallel operation of distributed generation inverters using resistive output impedance, IEEE Transactions on Industrial Electronics 54 (2) (2007) 994–1004. doi:10.1109/TIE.2007.892621.

[4] Q. C. Zhong, Y. Zeng, Universal droop control of inverters with different types of output impedance, IEEE Access 4 (2016) 702–712. doi:10.1109/ACCESS.2016.2526616.

[5] X. H. T. Pham, Power sharing strategy in islanded microgrids using improved droop control, Electric Power Systems Research 180 (2020) 106164. doi:https://doi.org/10.1016/j.epsr.2019.106164.

[6] T. L. Vandoorn, J. D. M. De Kooning, B. Meersman, J. M. Guerrero, L. Vandevelde, Automatic power-sharing modification of p/v droop controllers in low-voltage resistive microgrids, IEEE Trans. Power Del. 27 (4) (2012) 2318–2325. doi:10.1109/TPWRD.2012.2212919.

[7] X. Yu, C. Cecati, T. Dillon, M. G. Simoes, The new frontier of smart grids, IEEE Industrial Electronics Magazine 5 (3) (2011) 49–63. doi:10.1109/MIE.2011.942176.

[8] G. Lou, W. Gu, Y. Xu, W. Jin, X. Du, Stability robustness for secondary voltage control in autonomous microgrids with consideration of communication delays, IEEE Transactions on Power Systems 33 (4) (2018) 4164–4178. doi:10.1109/TPWRS.2017.2782243.

[9] S. D'Arco, J. A. Suul, O. B. Fosso, A virtual synchronous machine implementation for distributed control of power converters in smartgrids, Electric Power Systems Research 122 (2015) 180–197. doi:https://doi.org/10.1016/j.epsr.2015.01.001.

[10] X. Hou, Y. Sun, W. Yuan, H. Han, C. Zhong, J. M. Guerrero, Conventional p-omega/q-v droop control in highly resistive line of low-voltage coverter-based ac microgrid, Energies 9(11) (943) (11 2016).

[11] J. Schiffer, R. Ortega, A. Astolfi, J. Raisch, T. Sezi, Conditions for stability of droop-controlled inverter-based microgrids, Automatica 50 (10) (2014) 2457 – 2469. doi:https://doi.org/10.1016/j.automatica.2014.08.009.

[12] J. Schiffer, T. Seel, J. Raisch, T. Sezi, Voltage stability and reactive power sharing in inverter-based microgrids with consensus-based distributed voltage control, IEEE Transactions on Control Systems Technology 24 (1) (2016) 96–109. doi:10.1109/TCST.2015.2420622.

[13] N. Pogaku, M. Prodanovic, T. Green, Modeling, Analysis and Testing of Autonomous Operation of an Inverter-Based Microgrid, IEEE Trans. Power Electron. 22 (2) (2007) 613–625. doi:10.1109/TPEL.2006.890003.

[14] A. Garces, Small-signal stability in island residential microgrids considering droop controls and multiple scenarios of generation, Electric Power Systems Research 185 (2020) 106371. doi:https://doi.org/10.1016/j.epsr.2020.106371.

[15] Z. Shuai, C. Shen, X. Yin, X. Liu, Z. J. Shen, Fault analysis of inverter-interfaced distributed generators with different control schemes, IEEE Transactions on Power Delivery 33 (3) (2018) 1223–1235. doi:10.1109/TPWRD.2017.2717388.

[16] M. A. Zamani, A. Yazdani, T. S. Sidhu, A control strategy for enhanced operation of inverter-based microgrids under transient disturbances and network faults, IEEE Transactions on Power Delivery 27 (4) (2012) 1737–1747. doi:10.1109/TPWRD.2012.2205713.

[17] H. Xin, L. Huang, L. Zhang, Z. Wang, J. Hu, Synchronous instability mechanism of p-f droop-controlled voltage source converter caused by current saturation, IEEE Transactions on Power Systems 31 (6) (2016) 5206–5207. doi:10.1109/TPWRS.2016.2521325.

[18] J. Jia, G. Yang, A. H. Nielsen, A review on grid-connected converter control for short-circuit power provision under grid unbalanced faults, IEEE Transactions on Power Delivery 33 (2) (2018) 649–661. doi:10.1109/TPWRD.2017.2682164.

[19] L. He, Z. Shuai, X. Zhang, X. Liu, Z. Li, Z. J. Shen, Transient characteristics of synchronverters subjected to asymmetric faults, IEEE Transactions on Power Delivery 34 (3) (2019) 1171–1183. doi:10.1109/TPWRD.2019.2906766.

[20] H. Wen, M. Fazeli, A low-voltage ride-through strategy using mixed potential function for three-phase grid-connected pv systems, Electric Power Systems Research 173 (2019) 271 – 280. doi:https://doi.org/10.1016/j.epsr.2019.04.039.

[21] A. D. Paquette, D. M. Divan, Virtual impedance current limiting for inverters in microgrids with synchronous generators, IEEE Transactions on Industry Applications 51 (2) (2015) 1630–1638. doi:10.1109/TIA.2014.2345877.

[22] S. Acharya, M. S. El-Moursi, A. Al-Hinai, A. S. Al-Sumaiti, H. H. Zeineldin, A control strategy for voltage unbalance mitigation in an islanded microgrid considering demand side management capability, IEEE Transactions on Smart Grid 10 (3) (2019) 2558–2568. doi:10.1109/TSG.2018.2804954.

[23] A. Gkountaras, S. Dieckerhoff, T. Sezi, Evaluation of current limiting methods for grid forming inverters in medium voltage microgrids, in: 2015 IEEE Energy Conversion Congress and Exposition (ECCE), 2015, pp. 1223–1230. doi:10.1109/ECCE.2015.7309831.

[24] N. Bottrell, T. C. Green, Comparison of current-limiting strategies during fault ride-through of inverters to prevent latch-up and wind-up, IEEE Trans. Power Electron. 29 (7) (2014) 3786–3797. doi:10.1109/TPEL.2013.2279162.

[25] Q. C. Zhong, G. C. Konstantopoulos, Current-limiting droop control of grid-connected inverters, IEEE Transactions on Industrial Electronics 64 (7) (2017) 5963–5973. doi:10.1109/TIE.2016.2622402.

[26] X. Lu, J. Wang, J. M. Guerrero, D. Zhao, Virtual-impedance-based fault current limiters for inverter dominated ac microgrids, IEEE Transactions on Smart Grid 9 (3) (2018) 1599–1612. doi:10.1109/TSG.2016.2594811.

[27] L. Huang, H. Xin, Z. Wang, K. Wu, H. Wang, J. Hu, C. Lu, A virtual synchronous control for voltage-source

converters utilizing dynamics of dc-link capacitor to realize self-synchronization, IEEE Journal of Emerging and Selected Topics in Power Electronics 5 (4) (2017) 1565–1577. doi:10.1109/JESTPE.2017.2740424.

[28] A. G. Paspatis, G. C. Konstantopoulos, Three-phase current-limiting droop controlled inverters operating in parallel, in: 2019 IEEE Milan PowerTech, 2019, pp. 1–6. doi:10.1109/PTC.2019.8810595.

[29] D. Baimel, J. Belikov, J. M. Guerrero, Y. Levron, Dynamic modeling of networks, microgrids, and renewable sources in the dq0 reference frame: A survey, IEEE Access 5 (2017) 21323–21335. doi:10.1109/ACCESS.2017.2758523.

[30] G. C. Konstantopoulos, Q. C. Zhong, B. Ren, M. Krstic, Bounded integral control of input-to-state practically stable nonlinear systems to guarantee closed-loop stability, IEEE Transactions on Automatic Control 61 (12) (2016) 4196–4202. doi:10.1109/TAC.2016.2552978.

[31] H. K. Khalil, Nonlinear Systems, Prentice Hall, 1996.

[32] E. A. A. Coelho, D. Wu, J. M. Guerrero, J. C. Vasquez, T. Dragicevic, C. Stefanovic, P. Popovski, Small-signal analysis of the microgrid secondary control considering a communication time delay, IEEE Transactions on Industrial Electronics 63 (10) (2016) 6257–6269. doi:10.1109/TIE.2016.2581155.

[33] X. Wu, C. Shen, M. Zhao, Z. Wang, X. Huang, Small signal security region of droop coefficients in autonomous microgrids, in: 2014 IEEE PES General Meeting — Conference Exposition, 2014, pp. 1–5. doi:10.1109/PESGM.2014.6939139.

[34] D. Dheer, S. Doolla, S. Bandyopadhyay, J. M. Guerrero, Effect of placement of droop based generators in distribution network on small signal stability margin and network loss, International Journal of Electrical Power & Energy Systems 88 (2017) 108 – 118. doi:https://doi.org/10.1016/j.ijepes.2016.12.014.

[35] M. S. Golsorkhi, D. D. C. Lu, A control method for inverter-based islanded microgrids based on v-i droop characteristics, IEEE Transactions on Power Delivery 30 (3) (2015) 1196–1204. doi:10.1109/TPWRD.2014.2357471.